REVIEW

Check for updates

Methylamine gas healing of perovskite films: a short review and perspective

Lianzheng Hao,[ab] Qiangqiang Zhao,[c] Xiao Wang,[a] Shuping Pang [iD] *[a] and Guanglei Cui [iD] *[a]

The first challenge in the commercialization of perovskite solar cells (PSCs) is how to easily fabricate large-scale, high-quality perovskite films. Although some methods have been developed for the fabrication of large-scale films, the film quality still needs to be improved. The MA^0 healing method, as a post-processing technique, can be perfectly combined with other large-scale methods. However, determining the mechanism of the whole process is crucial for commercial production and subsequent research. Herein, we summarize the research progress on the MA^0 healing method. Firstly, we introduce the interaction during the liquification process including the interaction of amines with Pb^{2+}, the generation of hydrogen bonds, the influence of H_2O, and the reactions between different amines. Then, we systematically discuss the dynamic mechanism of adsorption and desorption. Finally, several aspects that need to be further clarified are proposed.

Introduction

Perovskite solar cells (PSCs) have attracted extensive attention from both the research community and industry due to their advantage of facile fabrication *via* solution method. Recently, the efficiency of solution-processed small-area PSCs has reached 25.5% certified by NREL,[1] while the certified module (802 cm^2) just reached 17.9%.[2] It remains a great challenge to simply fabricate large-scale, high-quality perovskite films and

PSCs with high consistency. Various methods have been developed to fabricate large-scale perovskite films, including but not limited to D-bar and blade coating,[3,4] slot-die coating,[5-8] spray coating,[9-14] dip coating,[6,15] and air-knife-assisted coating.[16] Generally, solution-processed perovskite polycrystalline films have large roughness and pin hole structures, which is one of the important reasons why the efficiency of the modules is far below that of the small-sized devices.

Considering the uniformity of the perovskite film, methylamine gas (MA^0) healing is one of the most promising methods due to its easy processing and high consistency.[17-22] The discovery of MA^0 healing method was inspired by the reversible transformation of $MAPbI_3$ perovskite phase during the MA^0 absorbing and degassing process.[21] Generally, the rough $MAPbI_3$ perovskite film with low coverage is visually translucent

[a] *Qingdao Institute of Bioenergy and Bioprocess Technology, Chinese Academy of Sciences, Qingdao 266101, P. R. China. E-mail: pangsp@qibebt.ac.cn*
[b] *Center of Materials Science and Optoelectronics Engineering, University of Chinese Academy of Sciences, Beijing 100049, P. R. China*
[c] *Qingdao University of Science and Technology, Qingdao 266042, P. R. China*

Lianzheng Hao received his BEng Degree from the School of Materials Science and Engineering, Qingdao University of Science and Technology in 2019. He is currently a Master's student in Prof. Guanglei Cui's group at Qingdao Institute of Bioenergy and Bioprocess Technology, Chinese Academy of Sciences. His current research focuses on perovskite materials and solar cells.

Lianzheng Hao

Shuping Pang joined the group of Prof. K. Müllen at the Max Planck Institute for Polymer Research (MPIP) and obtained his PhD Degree in September 2011. Then he moved back to China and worked as a Professor at the Qingdao Institute of Bioenergy and Bioprocess Technology (QIBEBT), Chinese Academy of Sciences (CAS). His current research focus is on photoelectric devices.

Shuping Pang

and matte. After quick exposure to MA^0, the film bleached, forming an intermediate liquid phase of $MAPbI_3 \cdot xMA^0$. Subsequently, $MAPbI_3 \cdot xMA^0$ could quickly return to the highly uniform dark perovskite phase when the MA^0 environment was removed.[17] A schematic diagram of this process is shown in Fig. 1a, and scanning electron microscope (SEM) images of the surface morphology before and after MA^0 healing are shown in Fig. 1b. This process is generally represented by the following equation:

$$MAPbI_3 + xMA^0 \rightarrow MAPbI_3 \cdot xMA^0 \rightarrow MAPbI_3 + xMA^0 \quad (1)$$
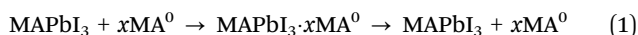
This method essentially belongs to post-processing technique and it hardly has high requirements for the initial film. Therefore, the MA^0 healing method can perfectly combine the above-mentioned large-scale methods to easily prepare large-sized, highly uniform and lattice-oriented $MAPbI_3$ films. Fig. 1c shows the $MAPbI_3$ module fabricated in the laboratory by this method, where the film has a mirror-smooth surface. Han *et al.* utilized the complex precursors of $MA^0 \cdot MAI$ and $MA^0 \cdot PbI_2$ combined with the pressure processing method to fabricate a 36.1 cm^2 $MAPbI_3$ module, reaching a PCE of 12.1%.[23] Park *et al.* applied D-bar coating to fabricate $MAPbI_3$ modules on an area of over 100 cm^2, reaching a PCE of 17.82% based on the MA^0-assisted $MAPbI_3$ solution.[3] The company Suzhou GCL Nano Co. Ltd successfully applied slot-die printing technology combined with MA^0 healing method to fabricate large-scale ($45 \times 65 \text{ cm}^2$) highly uniform $MAPbI_3$ films (Fig. 1d). In the initial stage, researches were mainly focused on how to fabricate high-quality perovskite films through this method. Qi *et al.* reported that introducing MA^0 in the annealing process can reduce impurities at the perovskite grain boundaries (GBs) and promote continuity between adjacent grains, and thus reduce defects at the GBs, reaching a high PCE of 18.4%.[24] Increasing the degassing temperature of the liquid–solid phase transition from $MAPbI_3 \cdot xMA^0$ to $MAPbI_3$ could also enhance the quality of the

Fig. 1 (a) Schematic diagram of the MA^0 healing process. (b) SEM micrographs of $MAPbI_3$ film before (top) and after (bottom) the MA^0 healing process. Copyright 2015 Wiley-VCH Verlag GmbH & Co. KGaA, Weinheim. (c) The $MAPbI_3$ module fabricated in the laboratory through MA^0 healing method. Copyright 2018 Springer Nature. (d) Large-sized $MAPbI_3$ film ($45 \times 65 \text{ cm}^2$) prepared by MA^0 healing method (provided by Suzhou GCL Nano Co. Ltd).

perovskite films with crystal grains in the order of tens of micrometers.[25] Additive engineering (such as MACl) is also compatible with the MA^0 healing method,[26] with the formation of a new intermediate phase, $MAPbI_3 \cdot MACl \cdot xMA^0$ (PCE = 19.4%). The transformation of the as-prepared $MAPbI_3$ thin film from $MAPbI_3 \cdot MACl \cdot xMA^0$ to $MAPbI_3$ is a two-step decomposition process, resulting in large, oriented grains spanning the film thickness and ultralow-density GB-network with only vertical GBs. Besides the gas healing of the rough $MAPbI_3$ perovskite films, MA^0 was also employed as a cosolvent with the mixing of acetonitrile (ACN) or DMF (PCE > 18%).[27–29] Recently, it was further discovered that extending the degassing time at an elevated temperature could increase the grain size, reaching millimeters (PCE = 21.36%).[30] Large-grain perovskite films possess a low trap-state density, long charge carrier lifetime, and excellent environmental stability. Through MA^0 healing treatment, the device stability also has great enhancement due to the improvement in film quality. For example, Qi *et al.* reported that unencapsulated PSCs retained 90% of their initial efficiency after 800 h continuous light illumination under an N_2 atmosphere, while the control device decayed to 90% of its initial efficiency in just 300 h.[31] Song *et al.* reported that $MAPbI_3$ devices fabricated using the optimized MA^0 healing method with ultra-large grains retained 85% of their initial PCEs under illumination after 1000 h in an N_2 atmosphere, whereas control devices decayed to about 60% of their original PCEs.[30] Due to the high uniformity of the perovskite films and the device consistency, this MA^0 healing method represents a major advance in the scale-up fabrication of high-quality perovskite films and devices.[3,22,23,31–34] **However, the limitation of the MA^0 healing method is that it cannot be used for the $FAPbI_3$** Recently, some research groups have started studying the related mechanisms of the whole process.[35–37]

Guanglei Cui received his PhD Degree from the Institute of Chemistry, CAS, in 2005. He then conducted postdoctoral research at the Max Planck Institute for Polymer Research and Solid States Research before joining QIBEBT, CAS, in 2009. He is currently a Professor and Leader of the Biomimetics for Energy Storage group, Director of the Applied Energy Technology Division, and Deputy Director of the Academic Committee of the QIBEBT. His research topics include sustainable and highly efficient energy-storage materials, all-solid-state batteries, and novel energy devices.

Guanglei Cui

This journal is © The Royal Society of Chemistry 2022

J. Mater. Chem. C, 2022, **10**, 2390–2399 | **2391**

Herein, we summarize the research progress of the MA^0 healing method. This process can be divided into two segments, namely, liquification and recrystallization. In the case of the liquification process, we summarize the internal chemical interaction, which mainly include the interaction of amines with Pb^{2+}, the generation of hydrogen bonds, the influence of H_2O and the reactions between different amines. For the recrystallization process, the dynamic mechanism of adsorption and desorption is systematically discussed. Finally, we propose several issues that need to be further investigated.

The internal chemical interaction

The liquification of perovskite materials in MA^0 atmosphere is the basis of gas-healing technology. The understanding of underlying chemical reaction and intermolecular interaction is constantly being updated. Initially, Zhou et al.[17] supposed that the lone-electron pair in the nitrogen (N) atom of MA^0 molecules interacts with the PbI_6 octahedra, which leads to a liquefied state. Jen et al.[38] applied $MAPbBr_3$ and $MASnI_3$ as the raw film to determine whether the B-site metal ions and X-site halogen make a difference. The transformation phenomenon of $MAPbBr_3$ and $MASnI_3$ is very similar with $MAPbI_3$, which indicates that these two aspects are not determinant. Then, the interaction between $MAPbI_3$ and MA^0 was considered as a neutral ligand coordinated with the Pb(II) changing the three-dimensional lead halide framework.[39,40] Simultaneously, Rand et al.[41] reported that proton transfer occurs from PbI_2 to alkylamines, which results in the formation of $Pb–MA^0$ bonds and is responsible for the liquefaction. Also, the presence of an $MAPbI_3 \cdot xMA^0$ complex has also been proved by witnessing the Tyndall effect in this complex.[36,39,42,43] Cahoon et al.[44] supposed that the gas healing process should be interpreted as amino-deliquescence and amino-efflorescence, and the process of amino-deliquescence is driven by the highly exothermic dissolution of $MAPbI_3$ in MA^0. Some reports have indicated that the existence of hydrogen bonding between NH_3^+ in $MAPbI_3$ and NH_2 in MA^0 is also very significant.[35,36,39] The formation of MA^0– MA^+ dimers yields a situation comparable to ionic liquids, which

is also extremely important for the liquefaction of perovskite materials.[37] Thus, here we introduce the liquification process in detail.

(1) The reaction of amine and Pb^{2+}

MA^0 or other amine gases can not only liquify organic–inorganic perovskite structure, but also liquefy the PbI_2 structure.[23,39,41,45] Qi et al.[45] reported that MA^0 can penetrate the 2D layered structure of PbI_2 and react with the PbI_6^{4+} octahedra. Yan et al.[39] identified that the MA^0 molecules act as a type of ligand coordinating with Pb^{2+}. They supposed that the coordination was the filling of the empty lead 6p orbital $(6s^2 6p^2)$ by the lone electron pair from the nitrogen of MA^0 $(2s^2)$. The Pb–N binding energy calculated by first principles calculation is about 80.04 kJ mol^{-1}. Recently, Hillebrecht et al.[35,37] studied the structure of the intermediate phase and the change in chemical bonds in detail. They noted that there are actually two intermediate phases under the reversible reaction of MA^0 and $MAPbI_3$. When a stream of MA^0 passes over the PbI_2 or $MAPbI_3$ powder, a highly viscous liquid is formed, followed by pale-yellow platelets crystallized from it. Through the characterization of single-crystal X-ray diffraction, they obtained a neutral octahedral complex-$(MA^0)_4PbI_2$. As shown in Fig. 2a, in this structure, it can be seen that four MA^0 molecules act as the classical donor ligand to Pb^{2+}, and the two iodine anions exist in a *cis*-position. If a stronger MA^0 stream is injected from a cold trap, the PbI_2 or $MAPbI_3$ powder quickly liquefies and colorless crystals are precipitated from it. This colorless crystal is a type of new intermediate phase, which is stable at room temperature if it is kept in a closed vial with pure MA^0 as an equilibrium gas phase. The direct measurement of the crystal indicated the existence of multiple twinning. Through further structure refinement of the cubic data, they found that its structure model is the well-known K_2PtCl_6 type[46] with octahedral $[Pb(MA^0)_6]^{2+}$ complexes and isolated I^- anions (Fig. 2b). In this structure, Pb^{2+} is only surrounded by the neutral MA^0 ligand. When the MA^0 is gradually evaporated, $[Pb(MA^0)_6]I_2$ can be converted to $(MA^0)_4PbI_2$. The above-mentioned crystal structures provide a crucial basis for
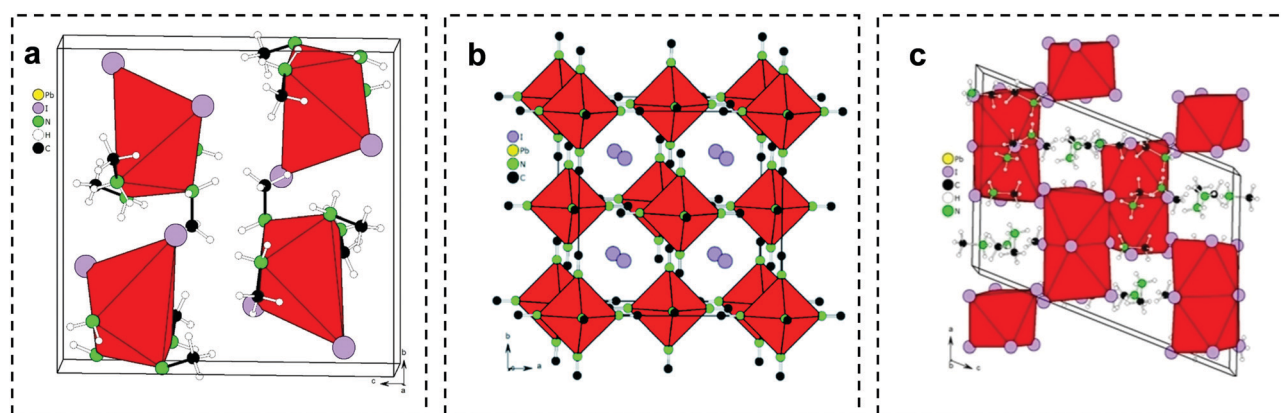

Fig. 2 (a) Crystal structure of $(MA^0)_4PbI_2$. Copyright 2021 Wiley-VCH GmbH. (b) Crystal structure of $[Pb(MA^0)_6]I_2$. Copyright The Royal Society of Chemistry 2020. (c) Crystal structure of $(MA)_5(MA^0)_2Pb_2I_9$ in (010) direction. Copyright 2021 Wiley-VCH GmbH.

understanding the interaction between MA^0 and the inorganic framework in perovskite materials. The formation of the liquid state is due to the fact that the MA^0 molecules coordinate with Pb^{2+} as the ligand destroys the initial perovskite crystal structure, and then change its physical state, but there is no evidence that the MA^0 healing of perovskite films pass through $[Pb(MA^0)_6]I_2$ and $(MA^0)_4PbI_2$ to $MAPbI_3$ finally. Therefore, other liquid intermediates should exist with a disordered structure, which coordinate with a different number of MA^0 molecules.

(2) The interaction of MA^0 and MA^+ (generation of hydrogen bonds)

The crystal structure of $MAPbI_3$ can be regarded as $[PbI_6]^{4-}$ octahedra in three-dimensional (3D) space, where the MA^+ ions fill the gaps among the octahedra.[47–49] Some experiments found that organic iodides such as MAI and MACl could also absorb MA^0 to form a liquid phase, which is much faster than that in perovskite materials.[26,43,50] Thus, the interaction between MA^0 and MA^+ cannot be ignored. Zheng et al.[36] confirmed the existence of MA^0–MA^+ dimers by applying ^{1}H NMR. They dispersed $MAPbI_3$ powder, MA^0–$MAPbI_3$ crystals and MA^0 in DMSO-d_6 for room-temperature ^{1}H NMR measurements. As shown in Fig. 3a, the ^{1}H NMR signals of $MAPbI_3$ appeared at 7.47 and 2.38 ppm, corresponding to the resonance of the

protons adjacent to nitrogen and carbon, respectively, while the ^{1}H NMR signal of the MA^0–$MAPbI_3$ sample appeared at 4.51 ppm, which is halfway between 7.47 ppm for $MAPbI_3$ and 1.06 ppm for MA^0. They attributed this chemical shift to the hydrogen bonding between NH_3^+ in $MAPbI_3$ and NH_2 in MA^0. The formation of hydrogen bonding was also verified by temperature-dependent ^{1}H NMR, as shown in Fig. 3b. The negative correlation between hydrogen bonds and temperature agrees well with the fact that the strength of hydrogen bonding is diminished at elevated temperature.[51,52] They also found a similar phenomenon in the MA^0–$MAPbCl_3$ and MA^0–$MAPbBr_3$ systems. The diameter of the MA^0–MA^+ dimers is 445 pm, which is about twice that of MA (217 pm). This will easily cause the collapse of the 3D perovskite structures.[53]

Around the same time, Andreas Hinsch et al. also confirmed the existence of MA^0–MA^+ dimers through Raman spectra.[35] They exposed the MA^0–$MAPbI_3$ complex in the air and measured the change in peaks in the Raman spectra. The only band at 290 cm^{-1} in the liquid state under high pressure (Fig. 3c) is related to the rotational mode of MA^+, which is in agreement with the result from Park et al.[3] This rotational mode is normally inactive, and the detectable rotational mode of MA^+ can be attributed to the lower local symmetry of the PbI_3 framework or the formation of MA^0–MA^+. During the process of MA^0 evaporation, the MA^+ rotational mode gradually disappeared.[54] In addition, the bands representing the CH_3–NH_3 rocking and C–N stretching vibrations of the free MA^+ under vacuum[55] gradually vanished during crystallization, as shown in Fig. 3c. These results demonstrate the existence of MA^0–MA^+ dimers. According to the above-mentioned two types of reaction, the liquification of $MAPbI_3$ may be driven by two effects, MA^0 bonding to Pb^{2+} atom via the lone electron pair along with the formation of MA^0–MA^+ dimers. Thus, the chemical reaction for liquification can be described as follows:

$$MAPbI_3 + xMA^0 \rightarrow Pb(MA^0)_{x-1}I_2 + [MA^0-MA]^+I^- \qquad (2)$$
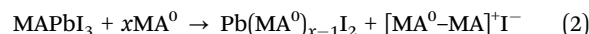
(3) The influence of H_2O

MA^0 healing is normally performed in a dry environment, which is due to the negative effect of H_2O on the film quality. Qi et al.[45] reported that PbI_2 can be converted to $MAPbI_3$ in the presence of H_2O during the reaction of PbI_2 and MA^0. Hillebrecht et al.[35] also studied this reaction, and they reported that H_2O could react with MA^0 to produce MA^+ cations and OH^- anions, generating a new compound, $[(MA)_5(MA^0)_2Pb_2I_9]$, in the MA^0 healing process. This compound contains $[Pb_2I_9]^{5+}$ units with two face-sharing octahedra and MA^0–MA^+ dimers bridged by a hydrogen bond (Fig. 2c). The charge balance of the system is achieved by MA^+ and the dimeric $(MA^0$–$MA)^+$ cations. $(MA)_5(MA^0)_2Pb_2I_9$ will convert to $MAPbI_3$ by further degassing, but $Pb(OH)I$ remains on the film as a by-product. Walsh et al. analyzed the effect of H_2O on the decomposition of $MAPbI_3$. They found that the kinetic barrier of I-ion migration was greatly reduced and all types of vacancy defects were easier to create deep transition levels in the presence of water. These effects could aggravate the decomposition of the perovskite.[56]
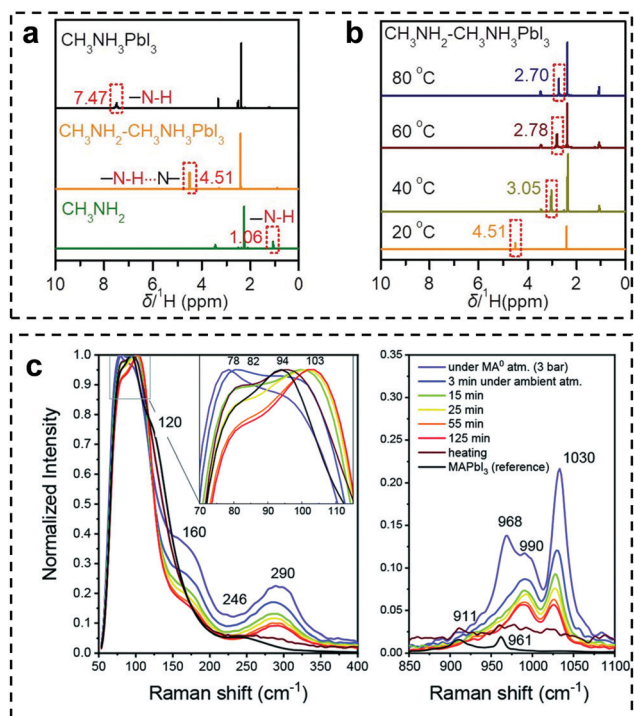

Fig. 3 (a) ^{1}H NMR spectra of $MAPbI_3$ powder, MA^0–$MAPbI_3$ crystals and MA^0 dispersed in DMSO-d_6. (b) Temperature-dependent ^{1}H NMR spectra of MA^0–$MAPbI_3$ crystals dispersed in DMSO-d_6. The NMR tube with the precursor sample was heated from 20 °C to 80 °C and tested at the corresponding temperatures in situ. Copyright 2020, the American Chemical Society. (c) Raman spectra of a liquified $MAPbI_3$·xMA^0 complex during liquid–solid conversion as the MA^0 leaves the complex. Copyright The Royal Society of Chemistry, 2020.

This journal is © The Royal Society of Chemistry 2022

J. Mater. Chem. C, 2022, **10**, 2390–2399 | **2393**

These results emphasize the importance of avoiding humidity during the MA^0 healing process, and the liquification process can be represented by eqn (3) with the existence of H_2O.

$$4MAPbI_3 + 4MA^0 + 2H_2O \rightarrow (MA)_5(MA^0)_2Pb_2I_9 + 2Pb(OH)I + MAI \quad (3)$$
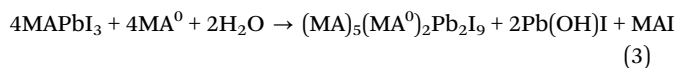
(4) The reactions between different amines

(i) Substitution reaction between different amines. Initially, Zhou *et al.* reported that ethylamine ($C_2H_5NH_2$) or *n*-butylamine ($CH_3(CH_2)_3NH_2$) can liquefy MAPbI$_3$ films, but the film cannot completely recover to the MAPbI$_3$ perovskite phase after the degassing process.[17] Thus, they gave the following equation:

$$MAI + R-NH_2 \rightarrow R-NH_3I + MA^0 \quad (4)$$

Then Zong *et al.*[57] transformed a rough, polycrystalline NH$_4$PbI$_3$ non-perovskite thin film into a dense, ultrasmooth, textured MAPbI$_3$ perovskite thin film through the MA^0 healing process. It is interesting that the yellow NH$_4$PbI$_3$ film initially converts to a black MAPbI$_3$ phase rather than being liquefied directly, and then transforms to MAPbI$_3$·xMA^0 under the MA^0 environment (Fig. 4a). The whole reaction process can be described by the following two equations:

$$NH_4PbI_3 + MA^0 \rightarrow MAPbI_3 + NH_3 \quad (5)$$

$$MAPbI_3 + xMA^0 \rightarrow MAPbI_3 \cdot xMA^0 \rightarrow MAPbI_3 + xMA^0 \quad (1)$$
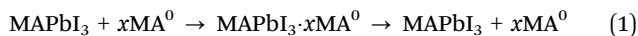
Simultaneously, Pang *et al.*[58] replaced NH$_4$PbI$_3$ with "HPbI$_3$" ((CH$_3$)$_2$NH$_2$PbI$_3$)[59,60] to fabricate high-quality MAPbI$_3$ films.

It is clear that $(CH_3)_2NH_2PbI_3$ (DMAPbI$_3$) is directly liquefied (Fig. 4b), which is different from the behavior of the NH$_4$PbI$_3$ crystals in the MA^0 environment. Thus, the reaction can be described as the following equation:

$$DMAPbI_3 + xMA^0 \rightarrow DMAPbI_3 \cdot xMA^0 \rightarrow MAPbI_3$$
$$+ (x-1)MA^0 + DMA \quad (6)$$
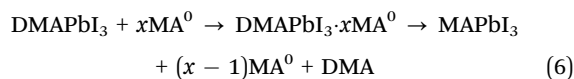
Actually, the conversion of organic–inorganic hybrid perovskites depends on the environment they are kept in. If a type of amine (monoamine) is adequate in the environment, the perovskite will be converted to the corresponding amine structure. The transformation time depends on the volatilization of the amine in the initial perovskite structure. For example, Wang *et al.*[61] confirmed that MAPbI$_3$, BA$_2$PbI$_4$, and OA$_2$PbI$_4$ can transform into each other in the corresponding A site cation gas environment. Chen *et al.*[62] also reported the mutual transformation of MAPbI$_3$ and EAPbI$_3$. Raga *et al.*[45] gave the transformation of different halide perovskites, as shown in Fig. 4c.

(ii) Addition–elimination reaction. Formamidinium lead iodide (FAPbI$_3$) has become the most widely studied light-absorbing perovskite material, which is ascribed to its suitable bandgap. However, the FAPbI$_3$ perovskite phase cannot be obtained by the MA^0 healing method, and its underlying mechanism remained unclear for a long time. Zhou *et al.*[63] directly replaced MA$^+$ with FA gas at 150 °C, where FA^0 needed to be *in situ* prepared due to its instability. Moreover, the FA^0 molecules will form the *s*-triazine structure spontaneously by the addition–elimination reaction.[64] This high-temperature gas treatment is only a transformation
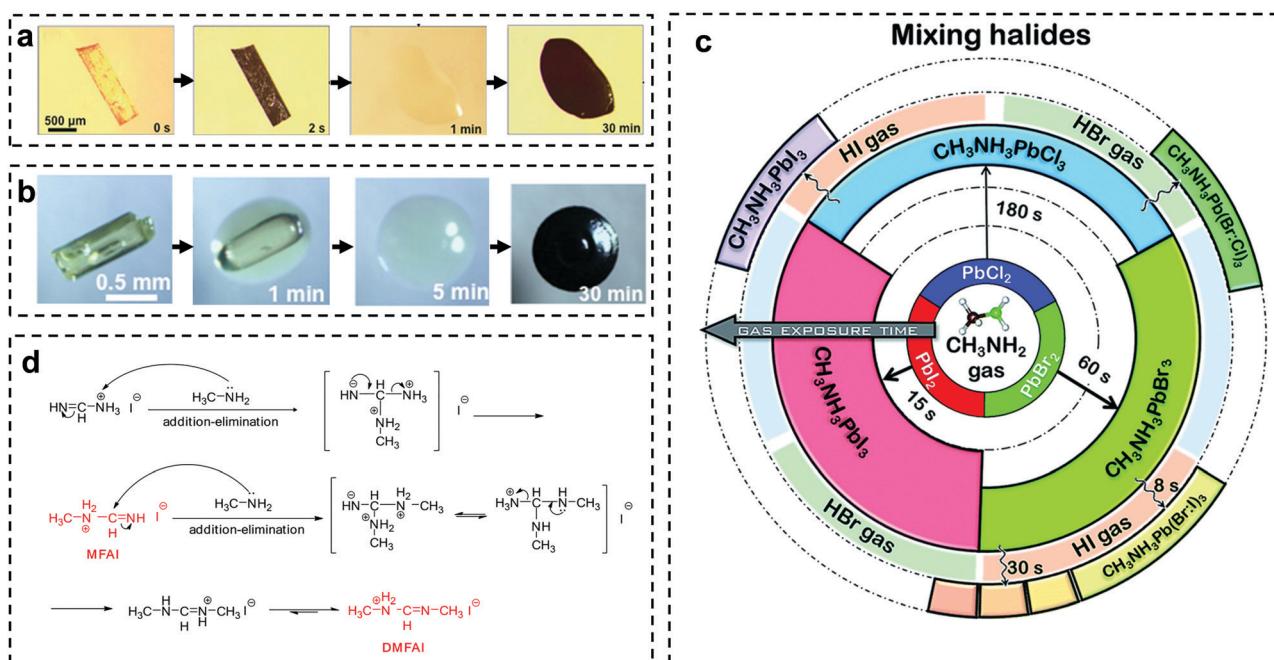

Fig. 4 (a) Optical photos of the morphological changes of NH$_4$PbI$_3$ crystal during the MA^0 healing process. Copyright 2016, the American Chemical Society. (b) Optical photos of the morphological changes of "HPbI$_3$" (DMAPbI$_3$) crystal during the MA^0 healing process. Copyright 2016, Wiley-VCH Verlag GmbH &Co. KGaA, Weinheim. (c) Perovskite conversion from PbX$_2$ (X = I, Br, and Cl) films exposed to MA gas and to HI and HBr gases. Copyright, The Royal Society of Chemistry, 2016. (d) Addition–elimination reactions between MA^0 and FAI. Copyright 2020, Elsevier Inc.

process without any modification of the film morphology. Zhang *et al.*[65] performed MA^0 healing on a mixed organic cation $MA_xFA_{1-x}PbI_3$ perovskite film, forming $MAPbI_3$ perovskite films with a second non-perovskite phase similar to the δ-$FAPbI_3$ structure. Recently,[66] Wang *et al.* discovered that FAI will undergo addition–elimination reactions with MA^0. The reaction mechanism of the reaction is shown in Fig. 4d. The lone-pair electrons of the N atom in MA^0 have nucleophilicity and the imine bond in FAI is an active electrophilic group, which leads to an addition–elimination reaction to form *N*-methyl formamidinium iodide (MFAI) and NH_3. Similarly, the formed MFAI also has an imine bond, which can undergo a second addition–elimination reaction with MA^0 to form *N*,*N'*-dimethyl formamidinium iodide (DMFAI). Therefore, the gas healing of the rough $FAPbI_3$- or FA-containing perovskite films to a highly uniform one is still a big challenge.

The dynamics of the recrystallization

During the MA^0 healing process, the next step is desorption-induced recrystallization of the perovskite film. Control of this step is also very important in the quality of perovskite films. Firstly, the absorption capacity determines the state of the intermediate and affects the subsequent recrystallization process. Then, the desorption of MA^0 affects the generation of a crystal nucleus and its growth process. Thus, it is necessary to determine the dynamic mechanism of these processes.

(1) Adsorption of MA^0 gas

The first factor affecting the adsorption capacity of $MAPbI_3$ to absorb MA^0 is the pressure. Jen *et al.*[38] observed that $MAPbI_3$ films preferred to completely liquefy under a high MA^0 pressure compared with low pressure. Under high MA^0 vapor pressure, the diffusion of MA^0 molecules could quickly break the physical bonds of the initial material (Fig. 5a). In contrast, under a low MA^0 vapor pressure, the diffusion of MA^0 is constrained to the initial physical extent (Fig. 5b). This is consistent with the conclusion of Hillebrecht *et al.*,[35] who found that the intermediate phase is $[Pb(CH_3NH_2)_6]I_2$ under high MA^0 vapor, and that under low MA^0 vapor pressure is $(CH_3NH_2)_4PbI_2$.

Temperature is another factor affecting the adsorbing capacity of $MAPbI_3$ films to absorb MA^0. Zang *et al.*[25] discovered the phenomenon that the liquid $MAPbI_3 \cdot xMA^0$ intermediate phase under steady MA^0 atmosphere still transform to solid state at elevated temperature. As shown in Fig. 5c, all the $MAPbI_3$ samples are exposed to nitrogen or MA^0 atmosphere maintained from 25 °C to 100 °C respectively. It is clear that high temperature is conducive to the degassing of perovskite films, appearing a black perovskite phase. When the temperature exceeds 55 °C, the liquid phase starts transitioning back to the solid state even under MA atmosphere. At 100 °C, no liquid intermediate phase exists.
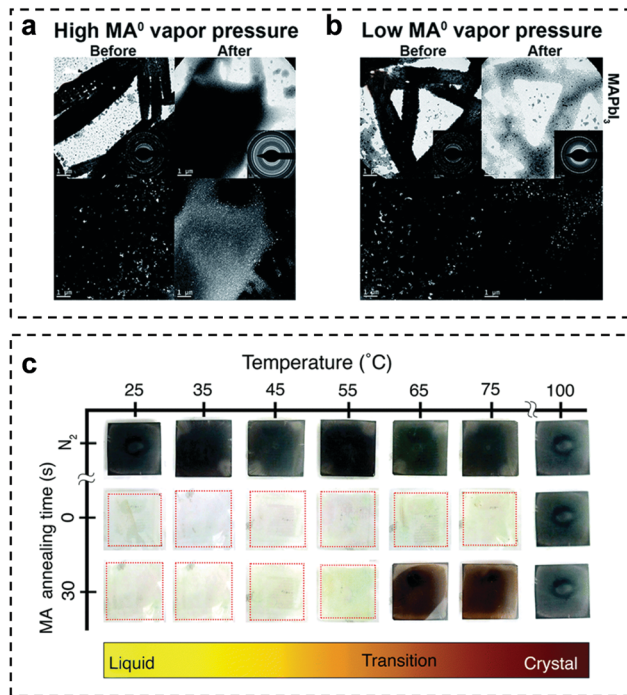

Fig. 5 TEM images of $MAPbI_3$ before and after exposure to MA^0 vapor. Each pane contains four pictures, the top line are the bright field images and select area electron diffraction (inset). The bottom line are the dark field images. (a) High MA^0 vapor pressure and (b) low MA^0 vapor pressure. Copyright, The Royal Society of Chemistry, 2016. (c) Temperature-dependent annealing of $MAPbI_3$ under MA gas atmosphere. First line: images of the films under an N_2 flow after 5 minutes. Second line: images of the films immediately after exposure to MA atmosphere. Third line: images of the samples after 30 seconds under a continual flowing MA atmosphere. Copyright, The Royal Society of Chemistry 2016.

(2) Desorption of MA^0 gas

Temperature also has a great effect on the degassing process. Zang *et al.*[25] heated the liquid phase at 100 °C under an MA^0 atmosphere and the grain size of the film reached tens of microns. Besides, the release speed of MA^0 is directly related to crystallization. Song *et al.*[30] studied the influence of the MA^0 release speed on the crystallization process from $MAPbI_3 \cdot xMA^0$ to $MAPbI_3$. In the traditional MA^0 gas healing process, the pressure of MA^0 quickly decreases (close to 0) by removing the MA^0 environment as soon as possible. The quick formation of supersaturation leads to the formation of massive nuclei and fine-grained (~ 100 nm in size) thin films. Thus, high super-saturation is detrimental to the formation of large grains. Accordingly, slowing the release speed of MA^0 molecules from the liquid intermediate could lead to a low nucleation density and long growth time of the grains. As shown in Fig. 6a, the grain size is strongly dependent on the release time. The degassing process was conducted at 120 °C, and the grain size increased to millimetres when the degassing time was 30 s. With a further increase in the degassing time, the grain size seemed to no longer expand. Besides, it has been proven that the as-prepared perovskite films possessed a (110)-uniaxial crystallographic orientation and small full width of half
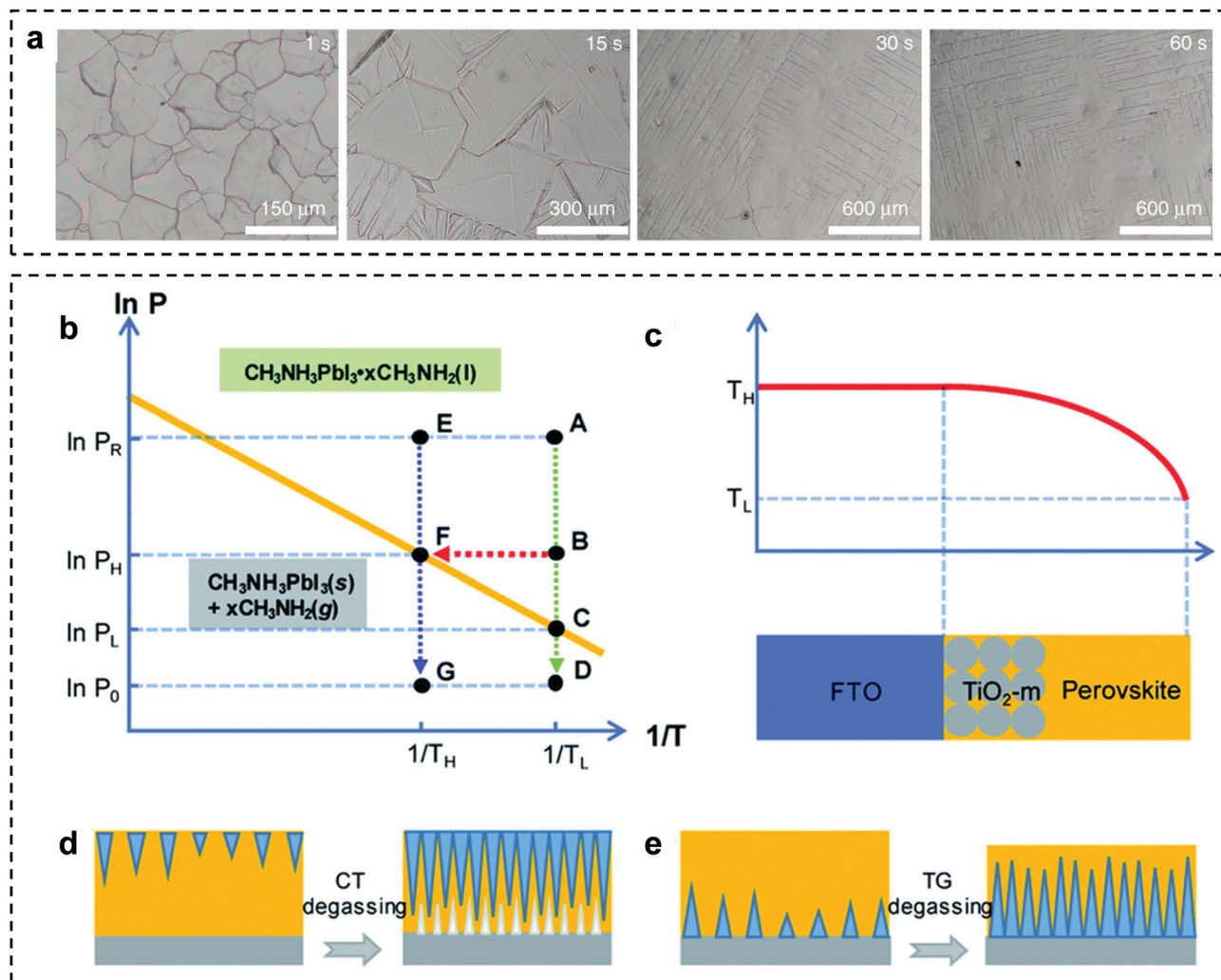
This journal is © The Royal Society of Chemistry 2022

J. Mater. Chem. C, 2022, **10**, 2390–2399 | **2395**

Fig. 6 (a) Optical microscopic images of the MAPbI$_3$ perovskite films prepared from the liquid intermediate with different degassing times (1, 15, 30, and 60 s). Copyright 2020, Springer Nature. (b) Thermodynamic model of the MA^0 desorption process. P_R is the pressure of MA^0 reacting with the perovskite film. P_0 is the actual pressure of the gas desorption process. (c) Diagram of the temperature gradient in the device. Schematic of the crystal growth model with (d) CT-MA (conventional MA^0 healing) method and (e) TG-MA (temperature gradient-induced MA^0 healing) method. Copyright The Royal Society of Chemistry, 2020.

maximum (FWHM), exhibiting a very low trap density, long carrier lifetime, and excellent environmental stability.

It is clear that the fast removal of the solvent can highly enhance the uniformity of perovskite films.[24,27,67,68] Considering this, in solar cell devices, the carrier transport is mainly in the vertical direction. The directional growth of the perovskite layer to form a grain structure in the through-thickness direction is necessary. According to the Clausius–Clapeyron equation[69,70] (Fig. 6b), the point on the oblique line represents that MAPbI$_3$· xMA^0 is in an equilibrium state. When the MA^0 pressure is lower than the value on the line, MAPbI$_3$·xMA^0 begins to degas. In the conventional MA^0 gas healing process at room temperature, the process from A to D happens instantaneously. Supersaturation is the driving force behind the crystallization, corresponding to the C–D process in Fig. 6b. After MA^0 is desorbed from the surface, the perovskite film starts the nucleation process from the surface and continues to nucleate

throughout the whole film, which will cause the formation of pinhole structures in the perovskite film (Fig. 6d). It is clear that the higher the temperature, the easier the desorption reaction will occur, as shown in Fig. 6b with the corresponding gas desorption process from E to G. In this case, a longitudinal temperature gradient (TG degassing) was formed to induce the directional growth of perovskite film.[71] The raw FTO/TiO$_2$/ MAPbI$_3$ substrate was preheated to 60 °C, and then subjected to the MA^0 healing process with cold MA^0. The surface temperature of the perovskite film quickly decreased, while the bottom of the film remained at a relatively higher temperature due to the large enthalpy of the glass substrate, as shown in Fig. 6c. It was proven that the crystallization started from the bottom of the film, and then grew upward, as shown in Fig. 6e, resulting in a reduction in defects in the perovskite film and improved carrier injection efficiency in the electron selective layer.

2396 | J. Mater. Chem. C, 2022, 10, 2390–2399

This journal is © The Royal Society of Chemistry 2022

Conclusion and outlook

In this review, we summarized the knowledge on the MA^0 healing method. Firstly, we introduced the internal chemical interaction. In the current perception, $MAPbI_3$ liquefaction may be driven by two effects, MA^0 bonding to the Pb^{2+} atom via its lone electron pair along with the formation of MA^0–MA^+. (Moreover, humidity should be avoided during the reaction, given that H_2O will participate in the reaction and produce $Pb(OH)I$ as the by-product. Also different types of $R–NH_2PbI_3$ can transform mutually if the corresponding amine is adequate.) Then, we introduced the dynamics of recrystallization. The temperature, MA^0 pressure, and release speed of MA^0 all have a great effect on the recrystallization. Although, the chemical basis of the reaction between MA^0 and $MAPbI_3$ is relatively clear, there are still some areas that are undefined and need further investigation.

1. In the process of industrial production, adequate fluidity is needed for the intermediate phase to repair the hole defect in the initial film. We mentioned above that the MA^0 molecule, acting as a ligand, coordinates with Pb_2^+. However, the influence of the number of MA^0 molecules coordinated with Pb_2^+ on the viscosity and surface tension of the intermediate is still unclear. Thus, a detailed investigation on this will be helpful for industrial production.

2. It has been reported that some MA^0 molecules can remain at the grain boundary of the $MAPbI_3$ layers after the MA^0 healing treatment.[32] It is still unclear whether the MA_0 molecules are embedded in the lattice and their impact on the long-term stability of the encapsulated devices.

3. There are some pathways to obtain large grain films such as increasing the temperature, retarding the degassing speed, and adding additives. The obtained perovskite film normally has large grains and excellent uniaxial orientation. However, whether each grain is a single crystal is still under debate. Thus, the defect density in the large gains should be further investigated.

4. Recently, FA-rich perovskite materials have been shown to be more stable and highly efficient photovoltaic materials. However, direct MA^0 gas healing to repair $FAPbI_3$ materials is not feasible due to the reaction between FAI and MA^0, and there are also difficulties in repairing $FAPbI_3$ materials through direct FA^0 healing due to the instability of FA^0. Therefore, a suitable gas healing method for FA-containing perovskite films is still lacking.

Conflicts of interest

There are no conflicts to declare.

Acknowledgements

References

1 N. R. E. Laboratory, Best research-cell efficiency chart https://www.nrel.gov/pv/cell-efficiency.html.

2 N. R. E. Laboratory, Champion Photovoltaic Module Efficiency Chart, https://www.nrel.gov/pv/module-efficiency.html.

3 D.-N. Jeong, D.-K. Lee, S. Seo, S. Y. Lim, Y. Zhang, H. Shin, H. Cheong and N.-G. Park, ACS Energy Lett., 2019, 4, 1189–1195.

4 Y. Deng, X. Zheng, Y. Bai, Q. Wang, J. Zhao and J. Huang, Nat. Energy, 2018, 3, 560–566.

5 J.-E. Kim, Y.-S. Jung, Y.-J. Heo, K. Hwang, T. Qin, D.-Y. Kim and D. Vak, Sol. Energy Mater. Sol. Cells, 2018, 179, 80–86.

6 L. Huang, C. Li, X. Sun, R. Xu, Y. Du, J. Ni, H. Cai, J. Li, Z. Hu and J. Zhang, Org. Electron., 2017, 40, 13–23.

7 M. He, B. Li, X. Cui, B. Jiang, Y. He, Y. Chen, D. O'Neil, P. Szymanski, M. A. Ei-Sayed, J. Huang and Z. Lin, Nat. Commun., 2017, 8, 16045.

8 F. Ye, H. Chen, F. Xie, W. Tang, M. Yin, J. He, E. Bi, Y. Wang, X. Yang and L. Han, Energy Environ. Sci., 2016, 9, 2295–2301.

9 M. Park, W. Cho, G. Lee, S. C. Hong, M. C. Kim, J. Yoon, N. Ahn and M. Choi, Small, 2019, 15, e1804005.

10 W. C. Chang, D. H. Lan, K. M. Lee, X. F. Wang and C. L. Liu, ChemSusChem, 2017, 10, 1405–1412.

11 S. Das, B. Yang, G. Gu, P. C. Joshi, I. N. Ivanov, C. M. Rouleau, T. Aytug, D. B. Geohegan and K. Xiao, ACS Photonics, 2015, 2, 680–686.

12 Z. Liang, S. Zhang, X. Xu, N. Wang, J. Wang, X. Wang, Z. Bi, G. Xu, N. Yuan and J. Ding, RSC Adv., 2015, 5, 60562–60569.

13 J. H. Heo, M. H. Lee, M. H. Jang and S. H. Im, J. Mater. Chem. A, 2016, 4, 17636–17642.

14 D. K. Mohamad, J. Griffin, C. Bracher, A. T. Barrows and D. G. Lidzey, Adv. Energy Mater., 2016, 6, 1066994.

15 H. C. Liao, P. Guo, C. P. Hsu, M. Lin, B. Wang, L. Zeng, W. Huang, C. M. M. Soe, W. F. Su, M. J. Bedzyk, M. R. Wasielewski, A. Facchetti, R. P. H. Chang, M. G. Kanatzidis and T. J. Marks, Adv. Energy Mater., 2016, 7, 1601660.

16 L.-L. Gao, C.-X. Li, C.-J. Li and G.-J. Yang, J. Mater. Chem. A, 2017, 5, 1548–1557.

17 Z. Zhou, Z. Wang, Y. Zhou, S. Pang, D. Wang, H. Xu, Z. Liu, N. P. Padture and G. Cui, Angew. Chem., Int. Ed., 2015, 54, 9705–9709.

18 S. R. Raga, Y. Jiang, L. K. Ono and Y. Qi, Energy Technol., 2017, 5, 1750–1761.

19 C. Li, S. Pang, H. Xu and G. Cui, Solar RRL, 2017, 1, 1700076.

20 J.-a. Yang, T. Qin, L. Xie, K. Liao, T. Li and F. Hao, J. Mater. Chem. C, 2019, 7, 10724–10742.

21 Y. Zhao and K. Zhu, Chem. Commun., 2014, 50, 1605–1607.

22 Y. Zhou and N. P. Padture, ACS Energy Lett., 2017, 2, 2166–2176.

23 H. Chen, F. Ye, W. Tang, J. He, M. Yin, Y. Wang, F. Xie, E. Bi, X. Yang, M. Gratzel and L. Han, *Nature*, 2017, **550**, 92–95.

24 Y. Jiang, E. J. Juarez-Perez, Q. Ge, S. Wang, M. R. Leyden, L. K. Ono, S. R. Raga, J. Hu and Y. Qi, *Mater. Horiz.*, 2016, **3**, 548–555.

25 D. L. Jacobs and L. Zang, *Chem. Commun.*, 2016, **52**, 10743–10746.

26 F. Ji, S. Pang, L. Zhang, Y. Zong, G. Cui, N. P. Padture and Y. Zhou, *ACS Energy Lett.*, 2017, **2**, 2727–2733.

27 N. K. Noel, S. N. Habisreutinger, B. Wenger, M. T. Klug, M. T. Hörantner, M. B. Johnston, R. J. Nicholas, D. T. Moore and H. J. Snaith, *Energy Environ. Sci.*, 2017, **10**, 145–152.

28 A. J. Ramadan, N. K. Noel, S. Fearn, N. Young, M. Walker, L. A. Rochford and H. J. Snaith, *Chem. Mater.*, 2018, **30**, 7737–7743.

29 Z. Liu, J. Hu, H. Jiao, L. Li, G. Zheng, Y. Chen, Y. Huang, Q. Zhang, C. Shen, Q. Chen and H. Zhou, *Adv. Mater.*, 2017, **29**, 1606774.

30 H. Fan, F. Li, P. Wang, Z. Gu, J. H. Huang, K. J. Jiang, B. Guan, L. M. Yang, X. Zhou and Y. Song, *Nat. Commun.*, 2020, **11**, 5402.

31 Z. Liu, L. Qiu, E. J. Juarez-Perez, Z. Hawash, T. Kim, Y. Jiang, Z. Wu, S. R. Raga, L. K. Ono, S. Liu and Y. Qi, *Nat. Commun.*, 2018, **9**, 1–11.

32 K. Huang, C. Wang, C. Zhang, S. Tong, H. Li, B. Liu, Y. Gao, Y. Dong, Y. Gao, Y. Peng and J. Yang, *Org. Electron.*, 2018, **55**, 140–145.

33 L. Hong, Y. Hu, A. Mei, Y. Sheng, P. Jiang, C. Tian, Y. Rong and H. Han, *Adv. Funct. Mater.*, 2017, **27**, 1703060.

34 Z. Shao, Z. Wang, Z. Li, Y. Fan, H. Meng, R. Liu, Y. Wang, A. Hagfeldt, G. Cui and S. Pang, *Angew. Chem., Int. Ed.*, 2019, **58**, 5587–5591.

35 D. Bogachuk, L. Wagner, S. Mastroianni, M. Daub, H. Hillebrecht and A. Hinsch, *J. Mater. Chem. A*, 2020, **8**, 9788–9796.

36 X. Huang, R. Chen, G. Deng, F. Han, P. Ruan, F. Cheng, J. Yin, B. Wu and N. Zheng, *J. Am. Chem. Soc.*, 2020, **142**, 6149–6157.

37 M. Daub and H. Hillebrecht, *Eur. J. Inorg. Chem.*, 2021, 1490–1497.

38 T. Zhao, S. T. Williams, C.-C. Chueh, D. W. deQuilettes, P.-W. Liang, D. S. Ginger and A. K. Y. Jen, *RSC Adv.*, 2016, **6**, 27475–27484.

39 M. Long, T. Zhang, H. Zhu, G. Li, F. Wang, W. Guo, Y. Chai, W. Chen, Q. Li, K. S. Wong, J. Xu and K. Yan, *Nano Energy*, 2017, **33**, 485–496.

40 X. Y. Feng, K. W. Ng, S. P. Wang, W. Z. Chen, Z. Z. Zhang, W. Chen, Y. Y. Zhao, B. Tu, Z. K. Tang, H. Pan and Z. B. He, *J. Mater. Chem. A*, 2020, **8**, 13585–13593.

41 R. A. Kerner, T. H. Schloemer, P. Schulz, J. J. Berry, J. Schwartz, A. Sellinger and B. P. Rand, *J. Mater. Chem. C*, 2019, **7**, 5251–5259.

42 C. Wu, H. Li, Y. Yan, B. Chi, J. Pu, J. Li, M. Sanghadasa and S. Priya, *Nano Energy*, 2017, **36**, 295–302.

43 R. G. Niemann, A. G. Kontos, D. Palles, E. I. Kamitsos, A. Kaltzoglou, F. Brivio, P. Falaras and P. J. Cameron, *J. Phys. Chem. C*, 2016, **120**, 2509–2519.

44 J. K. Meyers, L. Y. Serafin, A. D. Orr and J. F. Cahoon, *Chem. Mater.*, 2021, **33**, 3814–3822.

45 S. R. Raga, L. K. Ono and Y. Qi, *J. Mater. Chem. A*, 2016, **4**, 2494–2500.

46 R. Eßmann, G. Kreiner, A. Niemann, D. Rechenbach, A. Schmieding, T. Sichla, U. Zachwieja and H. Jacobs, *Z. Anorg. Allg. Chem.*, 1996, **622**, 1161–1166.

47 S. Luo and W. A. Daoud, *Materials*, 2016, **9**, 123.

48 X. Guo, C. McCleese, C. Kolodziej, A. C. Samia, Y. Zhao and C. Burda, *Dalton Trans.*, 2016, **45**, 3806–3813.

49 M. W. Lufaso and P. M. Woodward, *Acta Crystallogr., Sect. B: Struct. Sci.*, 2001, **57**, 725–738.

50 Y. Chang, L. Wang, J. Zhang, Z. Zhou, C. Li, B. Chen, L. Etgar, G. Cui and S. Pang, *J. Mater. Chem. A*, 2017, **5**, 4803–4808.

51 S. H. Gellman, G. P. Dado, G. B. Liang and B. R. Adams, *J. Am. Chem. Soc.*, 1991, **113**, 1164–1173.

52 E. D. Walter, L. Qi, A. Chamas, H. S. Mehta, J. A. Sears, S. L. Scott and D. W. Hoyt, *J. Phys. Chem. C*, 2018, **122**, 8209–8215.

53 W.-J. Yin, J.-H. Yang, J. Kang, Y. Yan and S.-H. Wei, *J. Mater. Chem. A*, 2015, **3**, 8926–8942.

54 C. Quarti, G. Grancini, E. Mosconi, P. Bruno, J. M. Ball, M. M. Lee, H. J. Snaith, A. Petrozza and F. D. Angelis, *J. Phys. Chem. Lett.*, 2014, **5**, 279–284.

55 T. Glaser, C. Muller, M. Sendner, C. Krekeler, O. E. Semonin, T. D. Hull, O. Yaffe, J. S. Owen, W. Kowalsky, A. Pucci and R. Lovrincic, *J. Phys. Chem. Lett.*, 2015, **6**, 2913–2918.

56 Y. H. Kye, C. J. Yu, U. G. Jong, Y. Chen and A. Walsh, *J. Phys. Chem. Lett.*, 2018, **9**, 2196–2201.

57 Y. Zong, Y. Zhou, M. Ju, H. F. Garces, A. R. Krause, F. Ji, G. Cui, X. C. Zeng, N. P. Padture and S. Pang, *Angew. Chem., Int. Ed.*, 2016, **55**, 14723–14727.

58 S. Pang, Y. Zhou, Z. Wang, M. Yang, A. R. Krause, Z. Zhou, K. Zhu, N. P. Padture and G. Cui, *J. Am. Chem. Soc.*, 2016, **138**, 750–753.

59 W. Ke, I. Spanopoulos, C. C. Stoumpos and M. G. Kanatzidis, *Nat. Commun.*, 2018, **9**, 4785.

60 M. Daub and H. Hillebrecht, *Z. Anorg. Allg. Chem.*, 2018, **644**, 1393–1400.

61 J. Wang, X. Yao, W.-J. Xiao, S. Wang, G. Xu, X.-Q. Chen, S.-C. Wu, I. Visoly-Fisher, E. A. Katz, Y. Li, J. Lin, W.-S. Li and Y. Li, *Solar RRL*, 2018, **2**, 1800125.

62 F. Wang, W. Li, H. Liu, L. Zhu and H. Chen, *Nanoscale*, 2019, **11**, 14465–14471.

63 Y. Zhou, M. Yang, S. Pang, K. Zhu and N. P. Padture, *J. Am. Chem. Soc.*, 2016, **138**, 5535–5538.

64 C. Chen, Y. Rao, Z. Li, X. Wang, G. Cui, W. Wang and S. Pang, *Solar RRL*, 2021, **5**, 2000715.

65 Y. Zhang, Z. Zhou, F. Ji, Z. Li, G. Cui, P. Gao, E. Oveisi, M. K. Nazeeruddin and S. Pang, *Adv. Mater.*, 2018, **30**, e1707143.

2398 | *J. Mater. Chem. C*, 2022, **10**, 2390–2399

This journal is © The Royal Society of Chemistry 2022

66 X. Wang, Y. Fan, L. Wang, C. Chen, Z. Li, R. Liu, H. Meng, Z. Shao, X. Du, H. Zhang, G. Cui and S. Pang, *Chemistry*, 2020, **6**, 1369–1378.

67 M. Long, T. Zhang, Y. Chai, C.-F. Ng, T. C. W. Mak, J. Xu and K. Yan, *Nat. Commun.*, 2016, **7**, 1–11.

68 T. Zhang, N. Guo, G. Li, X. Qian, L. Li and Y. Zhao, *J. Mater. Chem. A*, 2016, **4**, 3245–3248.

69 L. M. Wheeler, D. T. Moore, R. Ihly, N. J. Stanton, E. M. Miller, R. C. Tenent, J. L. Blackburn and N. R. Neale, *Nat. Commun.*, 2017, **8**, 1722.

70 V. Goetz and A. Marty, *Chem. Eng. Sci.*, 1992, **47**, 4445–4454.

71 L. Hao, Z. Li, L. Wang, R. Liu, Z. Shao, Z. Zhou, X. Guo, G. Cui, S. F. Liu and S. Pang, *J. Mater. Chem. A*, 2020, **8**, 17019–17024.

This journal is © The Royal Society of Chemistry 2022

J. Mater. Chem. C, 2022, **10**, 2390–2399 | **2399**